Check for updates

OPEN

Seismic constraints from a Mars impact experiment using InSight and Perseverance

Benjamin Fernando [1]✉, Natalia Wójcicka [2], Ross Maguire [3,4], Simon C. Stähler [5], Alexander E. Stott [6], Savas Ceylan [5], Constantinos Charalambous [7], John Clinton [5], Gareth S. Collins [2], Nikolaj Dahmen [5], Marouchka Froment [8,9], Matthew Golombek [10], Anna Horleston [11], Ozgur Karatekin [12], Taichi Kawamura [9], Carene Larmat [8], Tarje Nissen-Meyer [1], Manish R. Patel [13], Matthieu Plasman [9], Lilya Posiolova [14], Lucie Rolland [15], Aymeric Spiga [16,17], Nicholas A. Teanby [11], Géraldine Zenhäusern [5], Domenico Giardini [5], Philippe Lognonné [9], Bruce Banerdt [10] and Ingrid J. Daubar [18]

NASA's InSight (Interior Exploration using Seismic Investigations, Geodesy and Heat Transport) mission has operated a sophisticated suite of seismology and geophysics instruments on the surface of Mars since its arrival in 2018. On 18 February 2021, we attempted to detect the seismic and acoustic waves produced by the entry, descent and landing of the Perseverance rover using the sensors onboard the InSight lander. Similar observations have been made on Earth using data from both crewed[1,2] and uncrewed[3,4] spacecraft, and on the Moon during the Apollo era[5], but never before on Mars or another planet. This was the only seismic event to occur on Mars since InSight began operations that had an a priori known and independently constrained timing and location. It therefore had the potential to be used as a calibration for other marsquakes recorded by InSight. Here we report that no signal from Perseverance's entry, descent and landing is identifiable in the InSight data. Nonetheless, measurements made during the landing window enable us to place constraints on the distance–amplitude relationships used to predict the amplitude of seismic waves produced by planetary impacts and place in situ constraints on Martian impact seismic efficiency (the fraction of the impactor kinetic energy converted into seismic energy).

Pre-landing predictions based on modelling and on data from Mars Science Laboratory (Curiosity)'s entry, descent and landing (EDL) in 2012 suggested that the impact of the spacecraft's two cruise balance mass devices (CBMDs, also referred to as cruise mass balance devices, or CMBDs) might produce seismic waves of high enough amplitude to be detectable at the position of InSight (Interior Exploration using Seismic Investigations, Geodesy and Heat Transport), approximately 3,450 km to the east[6,7].

The CBMDs are solid, 77.5 kg tungsten blocks used to adjust the spacecraft's lift-to-drag ratio during EDL. Data from the spacecraft's computer indicate that the commands were generated to fire the pyrotechnic releases holding them in place at 20:28:27 UTC, within 1 s of each other. At this time, the spacecraft was projected to be at an altitude of 1,253 km and travelling at a planet-relative velocity of 4,753 m s^{-1}.

NASA's trajectory reconstruction indicates that the CBMDs hit the surface at $20{:}40{:}33 \pm 3$ s UTC (around five minutes before the rover's touchdown), at a speed of approximately 3,816 m s^{-1} and an oblique angle of around 10° from the horizontal.

The impact craters from the CBMDs were imaged by the CTX (Context Camera)[8] and HiRISE (High Resolution Imaging Science Experiment) instruments[9] on board NASA's Mars Reconnaissance Orbiter on 3 May 2021. Images identified the craters at a position around 18.9° N 76.2° E (Fig. 1).

The most promising candidate seismic phase for detection at InSight (4.5° N, 135.6° E) was expected to be a ballistic compressional (P) wave excited by the CBMD impact (Fig. 5 in ref. [7]). The P-wave arrival time was predicted to be approximately 420 ± 20 s after impact, or 20:47 UTC (19:50 InSight Local Mars Solar Time, LMST, on sol 793).

The two variables determining whether or not this signal would be identifiable in InSight data were the seismic noise during the arrival window (constrained after landing from the seismometer recordings), and the amplitude of the impact-induced P wave. The former was particularly low during the arrival window, as it occurred during the part of InSight's day when the atmospheric noise is lowest. The latter was predicted using distance–amplitude scaling curves[7,10,11]. These relationships come with large uncertainties, as they are calibrated using only terrestrial and lunar data at closer range.

[1]Department of Earth Sciences, University of Oxford, Oxford, UK. [2]Department of Earth Science and Engineering, Imperial College London, London, UK. [3]Department of Geology, University of Maryland, College Park, MD, USA. [4]Department of Computational Mathematics, Science, and Engineering, Michigan State University, East Lansing, MI, USA. [5]Department of Earth Sciences, ETH Zurich, Zurich, Switzerland. [6]Institut Supérieur de l'Aéronautique et de l'Espace (ISAE-SUPAERO), Toulouse, France. [7]Department of Electrical and Electronic Engineering, Imperial College London, London, UK. [8]Earth and Environmental Sciences Division, Los Alamos National Laboratory, Los Alamos, NM, USA. [9]Université de Paris, Institut de Physique du Globe de Paris, CNRS, Paris, France. [10]Jet Propulsion Laboratory, California Institute of Technology, Pasadena, CA, USA. [11]School of Earth Sciences, University of Bristol, Bristol, UK. [12]Royal Observatory of Belgium, Brussels, Belgium. [13]School of Physical Sciences, The Open University, Milton Keynes, UK. [14]Malin Space Science Systems, Inc., San Diego, CA, USA. [15]Laboratoire Géoazur, Université Côte d'Azur, Observatoire de la Côte d'Azur, CNRS, IRD, Sophia Antipolis, France. [16]Laboratoire de Météorologie Dynamique/Institut Pierre-Simon Laplace (LMD/IPSL), Sorbonne Université, Centre National de la Recherche Scientifique (CNRS), École Polytechnique, École Normale Supérieure (ENS), Paris, France. [17]Institut Universitaire de France (IUF), Paris, France. [18]Earth, Environment and Planetary Sciences, Brown University, Providence, RI, USA. ✉e-mail: benjamin.fernando@seh.ox.ac.uk
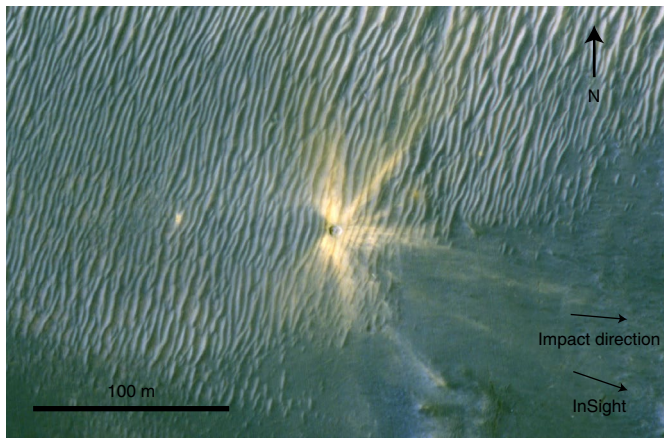
Fig. 1 | A high-resolution orbital image of one of the CBMD craters. This is the largest at ~6 m in diameter, and is located at 18.956° N, 76.202° E. This image is a crop of the enhanced colour HiRISE image with observation ID ESP_069231_1990. North is up, and illumination is from the left. Arrows indicate the direction of impact as inferred from the asymmetric ejecta pattern and the direction towards the InSight lander. The abundant aeolian ripples that trend north–south demonstrate that the surface materials are dominantly poorly consolidated and fine grained (sand), harnessed by the wind. Image: NASA/JPL/University of Arizona.

Data were recorded throughout the night (in UTC) of 18–19 February 2021 on InSight's Very Broad Band (VBB) seismometer[12], and the pressure and wind sensors of the Auxiliary Payload Sensor Suite (APSS)[13].

Data from the arrival window are plotted in Fig. 2. The main signals observed are a large marsquake around 01:25 UTC, and irregularly spaced glitches, which are artificial in origin. No other signal is observed that cannot be explained as noise excited by atmospheric phenomena, as corroborated using the wind speed and pressure measurements.

Therefore, we conclude that no signal associated with the CBMD impact is identifiable above the detection threshold (as defined in Fig. 2b), precluding a P-wave amplitude larger than $1.1 \times 10^{-10}\,\mathrm{m\,s^{-1}}$.

As the marsquake detected at 01:25 UTC fits within the projected time window (4–5 h after landing) for infrasound (low-frequency sound) waves to arrive from Perseverance's EDL, we will briefly outline why we believe it is unrelated and simply coincidental.

This assessment is based on the signal's amplitude, shape and frequency content, which are entirely different from those of an infrasound wave. EDL-related infrasounds at these distances should have amplitudes below the noise floor[7], whilst the high frequencies observed in this event (up to ~30 Hz) preclude an airborne propagation path, as the high CO_2 concentration in the Martian atmosphere would rapidly attenuate them[14]. Rather, this event ('S0794a') is a standard 'very high-frequency' marsquake[15], in this case with an origin at a distance of ~1,100 km, much closer than Perseverance. As of the end of April 2021, 40 of these events have been recorded by InSight, often in the late evening[16]. These events are probably caused by tectonic or otherwise internal geological processes.

Having established that there is no signal from the EDL recorded in the data, we will now consider what this non-detection can be used to infer about impact processes on Mars.

There are a number of approaches to using distance–amplitude scaling relationships to predict peak P-wave amplitudes from impacts.

Depending on whether the impactor energy, total momentum or vertical component of the momentum is used to scale the amplitude, and whether terrestrial missile-impact data or lunar

spacecraft-impact data are the basis, predicted amplitudes vary by up to two orders of magnitude when extrapolated to distances of 3,500 km. Five such standard scaling relationships are shown in Fig. 3—one based on impactor energy[10], and four based on impactor momentum[11].

Of the latter, two are based on data from artificial lunar impacts, which occurred into almost cohesionless material (black curves, ref. [5]), and two on terrestrial missile impacts into weakly cohesive regolith soils (green curves, ref. [17]). In each case, one curve uses the total impactor momentum as the determinant of peak P-wave amplitude (solid lines), whilst the other uses the vertical component of the impactor momentum (dashed lines).

The derived upper bound on the peak P-wave amplitude of $1.1 \times 10^{-10}\,\mathrm{m\,s^{-1}}$ is shown as a horizontal grey line in Fig. 3, and at the distance in question lies below the solid green scaling curve (total impactor momentum; terrestrial missile data).

This result indicates that the distance–amplitude scaling relationship based on terrestrial missile impacts into weakly cohesive soil, and the assumption that seismic wave amplitudes scale with total impactor momentum, are not appropriate in this case. There are three possible implications.

First, for highly oblique impacts such as this, this result suggests that the vertical component of the momentum may be a more appropriate quantity to scale by.

Alternatively, as the impact data on which this model was based were collected at much closer distances and on Earth, this may indicate a stronger attenuation of seismic wave amplitudes with distance on Mars. A third possibility is that artificial impacts on the lunar surface represent a better analogue for the seismic response of small impacts on Mars than those that occur into terrestrial soils.

The upper bound on the peak P-wave amplitude may be used to place a joint constraint on the impact seismic efficiency (k_s, which is site and impact specific) and the average mantle attenuation (Q_μ) along the path from Perseverance's landing site to InSight.

Because k_s and Q_μ are entirely independent of each other (the former being related to generation of seismic waves on a local scale, and the latter to their propagation on a global scale), jointly constraining their values in this way is valid.

k_s is particularly poorly constrained, due to its high sensitivity to local conditions and the lack of relevant in situ measurements[18]. All estimates for Mars thus far have therefore used modelling, simulation or material analogues to estimate its value, and no in situ measurements other than those in this paper exist.

Q_μ and Q_κ are the two quality factors used to describe viscoelastic (intrinsic/inelastic) attenuation properties within the solid part of the planet. The former is associated with shear properties, and the latter with bulk properties.

For typical Martian mantle rheologies, $Q_\mu \gg Q_\kappa$, hence Q_κ has little influence on P-wave amplitudes. The P-wave attenuation Q_P can then be approximated as $Q_P = \frac{9}{4}Q_\mu$.

Tidal observations suggest that Q_μ does not vary strongly through the mantle[19], so we assume that Q_μ is a reasonable descriptor of the average attenuation along the source–receiver path (Methods).

We do not treat the crust separately to the mantle, as the P-wave propagates almost entirely within the latter and previous studies show comparably negligible crustal attenuation[15,20]. To relate our observed upper bound on the P-wave amplitude to Q_μ and k_s, we first estimate the seismic moment associated with the CBMD impact using the following empirically derived relationship from ref. [21]:

$$M_0 = \frac{(k_s E_k)^{0.81}}{4.8 \times 10^{-9}} \tag{1}$$

where E_k is the impactor kinetic energy (in this case, 1.1 GJ). Note that the separation between the CBMDs in space and time at impact (~1 km and around 1 s) is large enough that the impact processes
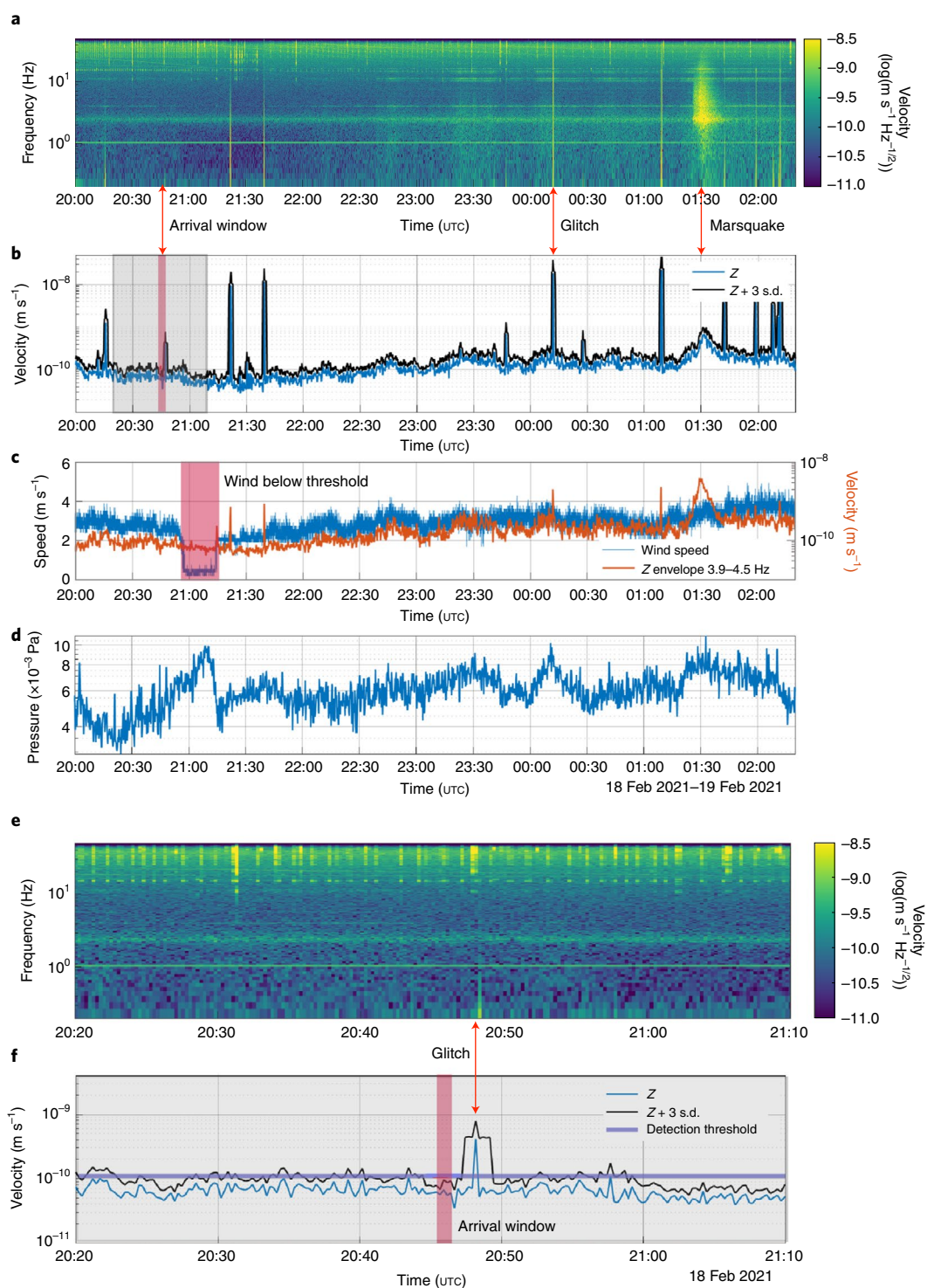
Fig. 2 | Data recorded by InSight during the landing window. a,b, A spectrogram of the vertical ground velocity recorded by the VBB seismometer (**a**) and the root mean square (r.m.s.) envelope of the vertical velocity in the 0.2–0.9 Hz frequency band most suited to isolating mantle-going phases (labelled Z) as well as the r.m.s. + 3 s.d. (**b**). In both panels, glitches in the system are recorded as sharp vertical features in the spectrogram and peaks in the r.m.s. envelope, with one exemplar highlighted. These glitches are easily distinguished from seismic signals[33]. The arrival window for the CBMD P wave is highlighted in red, as is an unrelated marsquake observed around 01:45 UTC. **c,** The wind speed and the r.m.s. envelope of the vertical seismometer velocity in the 3.9–4.5 Hz frequency band—the latter, in this frequency range, contains a known oscillation mode of the spacecraft, which is excited by the wind and can be used as a proxy for the wind speed[34]. The absence of wind measurements around 21:00 UTC occurs where the wind speed drops below the instrument threshold[13]. **d,** The r.m.s. envelope of the atmospheric pressure in the 0.1–4 Hz band, which is also correlated to wind speed[35]. **e,f,** A detail of the grey area in **a** and **b**, respectively, where the largest-amplitude event is a marked glitch just before 20:50 UTC, and our defined 'detection threshold' (an upper bound on the peak P-wave amplitude observed in the arrival window, defined as the r.m.s. of Z + 3 s.d.) is shown. Note that the LMST values corresponding to the left and right edges of **a–d** are 19:07 (sol 793) and 01:15 (sol 794).
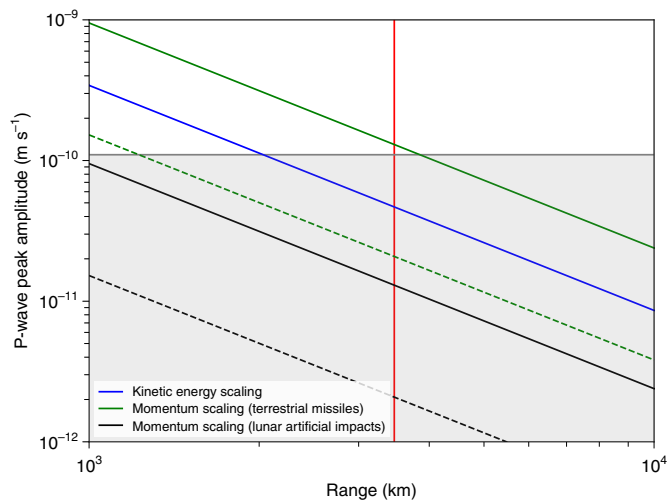
Fig. 3 | Predicted P-wave amplitudes for one CBMD impact calculated using different scaling relationships with distance from source. The ref. [10] scaling scales the amplitude with the square root of E_k (6×10^8 J). The ref. [11] scalings are based on either extrapolation of terrestrial missile impacts or lunar artificial impact data, using either total impact momentum (solid lines, $p = 3 \times 10^5$ N s) or the vertical component of impact momentum (dashed lines, $p_z = 4.8 \times 10^4$ N s) to scale the peak P-wave amplitude. The red vertical line marks the distance between the Perseverance landing site and the InSight lander. The horizontal grey line indicates the detection threshold with the grey shaded region indicating amplitudes below the threshold. Four of the five relationships are below the detection threshold, and one is above.

Fig. 4 | Constraints on k_s, given Q_μ, as derived from the non-observation of the CBMD impacts. Black curves are lines of constant amplitude, as would be recorded at InSight, and can be understood as either the line of valid k_s–Q_μ combinations if a P wave were observed with the specified peak amplitude, or the upper bound on k_s–Q_μ combinations if the noise floor were of this amplitude. Thus, k_s–Q_μ combinations in the red zone are precluded as they would require P-wave amplitudes above the noise floor. The orange zones are incompatible with the spectra of previously recorded marsquakes and estimates of the quality factor based on tidal excitations. The green zone shows the range of combinations that would satisfy these observations (although smaller values have been proposed previously, we only plot $k_s \geq 10^{-3}$, as this is the range of interest from these results). The rightmost point of this zone is 3% and marks the maximum possible value of k_s at this location on Mars.

occur independently of each other. E_k is thus the kinetic energy of a single CBMD.

As the P wave reduces in amplitude during its propagation through both attenuation and geometric spreading of the wavefront, making an estimate of Q_μ requires us to quantify the effects of the latter.

To do this, we undertook full-waveform seismic simulations using the AxiSEM method[22] in a purely elastic (non-attenuating) medium. Thus, the only energy loss in these simulations along the source–receiver path occurs due to the spreading of the wavefront. The effects of attenuation using an average Q_μ may then be applied as a post-simulation correction (Methods).

Now, the values of k_s and Q_μ may be independently varied (using equations (1) and (3), respectively) to determine their joint effect on the amplitude recorded by InSight.

Figure 4 shows joint constraints that may be placed on k_s for this impact scenario and Q_μ: as increasing the value of either parameter leads to larger predicted amplitudes, these are co-constrained such that the resultant P-wave amplitude does not exceed our detection threshold.

The quality factor has previously been determined to lie in the range 300–1,000, with the lower bound derived from tidal observations[19] and the upper from observations of the spectra of marsquakes[20,23]. Thus, we constrain the maximum value of k_s to be 3%, corresponding to the rightmost corner of the green zone in Fig. 4.

This upper limit on k_s is compatible with experimental (terrestrial and lunar) and simulated (terrestrial, lunar and Martian) measurements, where k_s ranges from 10^{-6} (in porous sand/regolith) to 10^{-3} (in stronger, non-porous materials)[5,11,17,24,25]. Values up to 2–3% have been observed in underground nuclear explosions in stronger target materials[26].

Figure 1 shows one of the impact craters. The surrounding morphology is representative of this region of Mars, and consists of aeolian bedforms and unconsolidated/poorly consolidated regolith. The thermal inertia of the surface at the impact location is
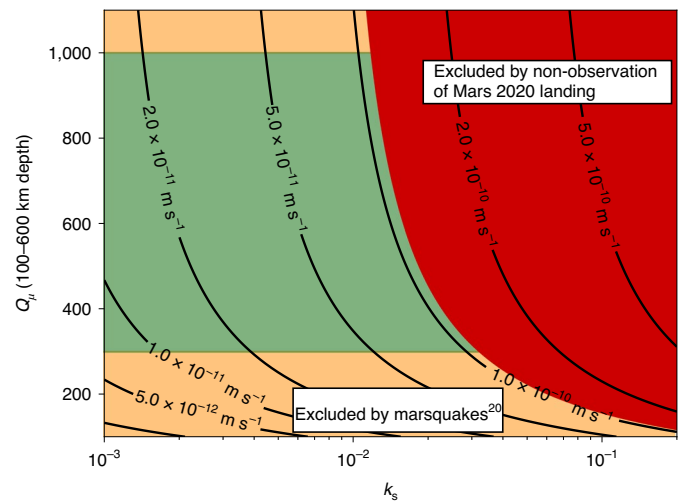
~250 J m^{-2} s$^{-1/2}$ K^{-1} (ref. [27]), indicative of a dominantly sandy surface. Although a quantitative relationship between k_s and target properties has yet to be derived, our upper bound on k_s is consistent with a surface material of this type.

The true seismic efficiency is likely to be lower than the maximum that we derived. Nonetheless, this does still demonstrate a practical method through which it may be constrained, and is notable that such a constraint has been derived on Mars. From this, we may draw the robust conclusion that the conversion of kinetic energy into seismic energy on Mars is no more efficient than the most efficient such terrestrial coupling.

We used the non-detection of the seismic waves from the impact of Perseverance's CBMDs to show that the total impactor momentum is a poor predictor of amplitude at this distance and impact angle, if a terrestrial-based scaling is assumed. In this case, the lunar-based scaling or a relationship based on impactor energy may be more appropriate. This result could also indicate that effects of attenuation on impact-generated seismic waves are stronger than previously estimated.

We also used the non-detection to constrain the impact seismic efficiency to be less than 3%, which is compatible with geological analysis of the impact site, and commensurate with previous estimates, which used modelling or proxies in place of in situ data.

The methodology presented here provides a basis for using seismic (non-)detection of artificial impacts to infer subsurface properties, and could in future be applied during geophysical missions to any of the Solar System's icy or rocky bodies.

Methods

We use an interior velocity and density model called 'TAYAK', which combines geochemical data with geodetic constraints[28,29]. This was chosen on the basis of its

good fit to other marsquake data[30]. The source is represented as an explosion just below the surface, as per ref. [18].

Simulations are conducted using the spectral element solver AxiSEM[22] in combination with Instaseis[31], with a dominant source period of 1 s, and with attenuation switched off. This allows us to account for amplitude decreases due to the geometric spreading of the wavefront.

Once the amplitude in the non-attenuating case A_0 (where $A_0 = A_0(M_0)$) has been found, we account for the effects of attenuation, assuming an effective $Q_{P,eff}$ that averages over the propagation path S:

$$Q_{P,eff}^{-1} = \int_S Q_P^{-1}(s) \, ds. \tag{2}$$

The amplitude in a frequency band between f_1 and f_2 (here 0.2 and 0.9 Hz) is estimated through application of the following equation:

$$A(Q_{P,eff}, M_0) = A_0(M_0) \frac{\int_{f_1}^{f_2} \exp\left(-\frac{tf}{2Q_{P,eff}}\right) df}{f_2 - f_1} \tag{3}$$

where A is the amplitude at InSight. Note that $Q_P = 9/4Q_\mu$, assuming a Poisson solid with a standard acoustic speed to shear speed ratio v_p/v_s of $\sqrt{3}$. $t = 420$ s is the predicted travel time of a P wave. Q is assumed to be frequency independent.

Combining equations (3), as derived above, and (1) allows us to determine which combinations of k_s and $Q_{P,eff}$ (and hence k_s and Q_μ) produce a permissible A at InSight's position, that is, one below the detection threshold.

Data availability

InSight APSS/TWINS/PS data can be found at https://atmos.nmsu.edu/data_and_services/atmospheres_data/INSIGHT/insight.html. InSight SEIS data are available in the form of a seismic event catalogue and waveform data (https://doi.org/10.18715/SEIS.INSIGHT.XB_2016) that are publicly available from the IPGP Data Center and IRIS-DMC, as well as raw data available in the PDS (https://pds-geosciences.wustl.edu/missions/insight/seis.htm). Data used here can be found in version 7 of the Mars Quake Service catalogue (https://doi.org/10.12686/a12). HiRISE data are publicly available through the Planetary Data System at https://www.uahirise.org/. Seismic modelling used the open-source Martian interior model TAYAK from refs. [29,32], available at https://instaseis.ethz.ch, and peak amplitudes were computed using the open-source AxiSEM method of ref. [22].

References

1. Hilton, D. & Henderson, H. Measurements of sonic boom overpressures from Apollo space vehicles. *J. Acoust. Soc. Am.* **56**, 323–328 (1974).
2. Qamar, A. Space shuttle and meteroid—tracking supersonic objects in the atmosphere with seismographs. *Seismol. Res. Lett.* **66**, 6–12 (1995).
3. Ishihara, Y., Hiramatsu, Y., Yamamoto, M., Furumoto, M. & Fujita, K. Infrasound/seismic observation of the Hayabusa reentry: observations and preliminary results. *Earth Planets Space* **64**, 655–660 (2012).
4. ReVelle, D. & Edwards, W. Stardust—an artificial, low-velocity 'meteor' fall and recovery: 15 January 2006. *Meteorit. Planet. Sci.* **42**, 271–299 (2007).
5. Latham, G. et al. Seismic data from man-made impacts on the moon. *Science* **170**, 620–626 (1970).
6. Bierhaus, E., McEwen, A., Wade, D. & Ivanov, A. A fortuitous impact experiment at Mars. In *44th Lunar and Planetary Science Conference* 2800 (LPI, 2013).
7. Fernando, B. et al. Listening for the landing: seismic detections of Perseverance's arrival at Mars with InSight. *Earth Space Sci.* **8**, e2020EA001585 (2021).
8. Malin, M. et al. Context camera investigation on board the Mars Reconnaissance Orbiter. *J. Geophys. Res. Planets* **112**, E05S04 (2007).
9. McEwen, A. et al. Mars Reconnaissance Orbiter's High Resolution Imaging Science Experiment (HiRISE). *J. Geophys. Res. Planets* **112**, E05S02 (2007).
10. Teanby, N. Predicted detection rates of regional-scale meteorite impacts on Mars with the InSight short-period seismometer. *Icarus* **256**, 49–62 (2015).
11. Wójcicka, N. et al. The seismic moment and seismic efficiency of small impacts on Mars. *J. Geophys. Res. Planets* **125**, e2020JE006540 (2020).
12. Lognonné, P. et al. SEIS: InSight's Seismic Experiment for Internal Structure of Mars. *Space Sci. Rev.* **215**, 12 (2019).
13. Banfield, D. et al. InSight Auxiliary Payload Sensor Suite (APSS). *Space Sci. Rev.* **215** (2019).
14. Bass, H. & Chambers, J. Absorption of sound in the Martian atmosphere. *J. Acoust. Soc. Am.* **109**, 3069–3071 (2001).
15. van Driel, M. et al. High-frequency seismic events on Mars observed by InSight. *J. Geophys. Res. Planets* **126**, e2020JE006670 (2021).
16. Clinton, J. et al. The Marsquake catalogue from InSight, sols 0-478. *Phys. Earth Planet. Inter.* **310**, 106595 (2021).
17. Latham, G., McDonald, W. & Moore, H. Missile impacts as sources of seismic energy on the Moon. *Science* **168**, 242–245 (1970).
18. Daubar, I. et al. Impact-seismic investigations of the InSight mission. *Space Sci. Rev.* **214**, 132 (2018).
19. Bagheri, A., Khan, A., Al-Attar, D., Crawford, O. & Giardini, D. Tidal response of Mars constrained from laboratory-based viscoelastic dissipation models and geophysical data. *J. Geophys. Res. Planets* **124**, 2703–2727 (2019).
20. Lognonné, P. et al. Constraints on the shallow elastic and anelastic structure of Mars from InSight seismic data. *Nat. Geosci.* **13**, 213–220 (2020).
21. Teanby, N. & Wookey, J. Seismic detection of meteorite impacts on Mars. *Phys. Earth Planet. Inter.* **186**, 70–80 (2011).
22. Nissen-Meyer, T. et al. AxiSEM: broadband 3-D seismic wavefields in axisymmetric media. *Solid Earth* **5**, 425–445 (2014).
23. Giardini, D. et al. The seismicity of Mars. *Nat. Geosci.* **13**, 205–212 (2020).
24. Richardson, J. & Kedar, S. An experimental investigation of the seismic signal produced by hypervelocity impacts. *Proc. Lunar Planet. Sci.* **44**, 2863 (2013).
25. Rajšić, A. et al. Seismic efficiency for simple crater formation in the Martian top crust analog. *J. Geophys. Res. Planets* **126**, e2020JE006662 (2021).
26. Patton, H. & Walter, W. Regional moment:magnitude relations for earthquakes and explosions. *Geophys. Res. Lett.* **20**, 277–280 (1993).
27. Putzig, N. & Mellon, M. Apparent thermal inertia and the surface heterogeneity of Mars. *Icarus* **191**, 68–94 (2007).
28. Clinton, J. et al. Preparing for InSight: an invitation to participate in a blind test for Martian seismicity. *Seismol. Res. Lett.* **88**, 1290–1302 (2017).
29. Khan, A. et al. A geophysical perspective on the bulk composition of Mars. *J. Geophys. Res. Planets* **123**, 575–611 (2018).
30. Brinkman, N. et al. First focal mechanisms of Marsquakes. *J. Geophys. Res. Planets* **126**, e2020JE006546 (2021).
31. van Driel, M., Krischer, L., Stähler, S., Hosseini, K. & Nissen-Meyer, T. Instaseis: instant global seismograms based on a broadband waveform database. *Solid Earth* **6**, 701–717 (2015).
32. Ceylan, S. et al. From initial models of seismicity, structure and noise to synthetic seismograms for Mars. *Space Sci. Rev.* **211**, 595–610 (2017).
33. Scholz, J. et al. Detection, analysis, and removal of glitches from InSight's seismic data from Mars. *Earth Space Sci.* **7**, e2020EA001317 (2020).
34. Ceylan, S. et al. Companion guide to the marsquake catalog from InSight, Sols 0-478: data content and non-seismic events. *Phys. Earth Planet. Inter.* **310**, 106597 (2021).
35. Charalambous, C. et al. A comodulation analysis of atmospheric energy injection into the ground motion at InSight, Mars. *J. Geophys. Res. Planets* **126**, e2020JE006538 (2021).

Author contributions

B.F., N.W., S.C.S., B.B., P.L. and I.J.D. designed the study and instrument operation plans. S.C., C.C., J.C., N.D., A.H., T.K., M.P., S.C.S. and G.Z. were responsible for frontline data analysis as part of the Marsquake Service. R.M., A.E.S., G.S.C., M.F., M.G., O.K., C.L., T.N.-M., L.R., A.S., N.A.T., D.G. and I.J.D. assisted with data interpretation and processing, and figure drafting. L.P., I.J.D. and M.R.P. were responsible for coordinating orbital imaging campaigns. This manuscript was written primarily by B.F., N.W. and S.C.S.

Competing interests

The authors declare no competing interests.

Additional information

Correspondence and requests for materials should be addressed to Benjamin Fernando.

Peer review information *Nature Astronomy* thanks Noah Petro and the other, anonymous, reviewers for their contribution to the peer review of this work.